Author/s:
Nguyen, CK;Taylor, PD;Zavabeti, A;Alluhaybi, H;Almalki, S;Guo, X;Irfan, M;Al Kobaisi, M;Ippolito, SJ;Spencer, MJS;Balendhran, S;Roberts, A;Daeneke, T;Crozier, KB;Sabri, Y;Syed, N

Title:
Instant-in-Air Liquid Metal Printed Ultrathin Tin Oxide for High-Performance Ammonia Sensors

Date:
2024

Citation:
Nguyen, C. K., Taylor, P. D., Zavabeti, A., Alluhaybi, H., Almalki, S., Guo, X., Irfan, M., Al Kobaisi, M., Ippolito, S. J., Spencer, M. J. S., Balendhran, S., Roberts, A., Daeneke, T., Crozier, K. B., Sabri, Y. & Syed, N. (2024). Instant-in-Air Liquid Metal Printed Ultrathin Tin Oxide for High-Performance Ammonia Sensors. Advanced Functional Materials, 34 (31), https://doi.org/10.1002/adfm.202309342.

Persistent Link:
https://hdl.handle.net/11343/339546

Instant-in-Air Liquid Metal Printed Ultrathin Tin Oxide for High-Performance Ammonia Sensors

Chung Kim Nguyen, Patrick D. Taylor, Ali Zavabeti, Hamidah Alluhaybi, Samira Almalki, Xiangyang Guo, Mehmood Irfan, Mohammad Al Kobaisi, Samuel J. Ippolito, Michelle J.S. Spencer, Sivacarendran Balendhran, Ann Roberts, Torben Daeneke, Kenneth B. Crozier, Ylias Sabri,* and Nitu Syed**

Liquid metal-based printing techniques are emerging as an exemplary platform for harvesting non-layered 2D materials with a thickness down to a few nanometres, leading to an ultra-large surface-area-to-volume ratio that is ideal for sensing applications. In this work, the synthesis of 2D tin dioxide (SnO_2) by exfoliating the surface oxide of molten tin is reported which highlights the enhanced sensing capability of the obtained materials to ammonia (NH_3) gas is reported. It is demonstrated that amperometric gas sensors based on liquid metal-derived 2D SnO_2 nanosheets can achieve excellent NH_3 sensing performance at low temperature (150 °C) with and without UV light assistance. Detection over a wide range of NH_3 concentrations (5–500 ppm) is observed, revealing a limit of detection at the parts per billion (ppb) level. The 2D SnO_2 nanosheets also feature excellent cross-interference performance toward different organic and inorganic gas species, showcasing a high selectivity. Further, ab initio DFT calculations reveal the NH_3 adsorption mechanism is dominated by chemisorption with a charge transfer into 2D SnO_2 nanosheets. In addition, a proof of concept for prototype flexible ammonia sensors is demonstrated by depositing 2D SnO_2 on a polyimide substrate, signifying the high potential of employing liquid metal printed SnO_2 for realizing wearable gas sensors.

1. Introduction

Electronic gas sensors are an integral part of our technological landscape, allowing us to detect pollutants, monitor processes, and ensure the safe operation of infrastructure and chemical production facilities.[1] With the continuous move toward a renewable economy, new challenges in the area of gas sensing are emerging. As society is moving away from fossil fuels, other molecules such as hydrogen (H_2) and ammonia (NH_3) are gaining significant importance as energy storage media and fuels.[2–5] The use of green ammonia is predicted to play a central role in the energy transition since it has a high volumetric energy density, can be decomposed into H_2 and N_2 with ease, and is thus touted as a promising energy carrier that can overcome the storage and transport challenges of hydrogen.[2] While ammonia is already used on vast scales, it is a highly toxic substance,[6–8] and introducing it into the transportation

C. K. Nguyen, A. Zavabeti, X. Guo, M. Irfan, S. J. Ippolito, T. Daeneke, Y. Sabri, N. Syed
School of Engineering
RMIT University
Melbourne, VIC 3001, Australia
E-mail: ylias.sabri@rmit.edu.au; nitu.syed@unimelb.edu.au

P. D. Taylor, M. J. S. Spencer
ARC Centre of Excellence in Future Low-Energy Electronics
School of Science
RMIT University
Melbourne, VIC 3001, Australia

A. Zavabeti
Department of Chemical Engineering
The University of Melbourne
Parkville, VIC 3010, Australia

H. Alluhaybi, S. Almalki, M. A. Kobaisi, S. J. Ippolito, Y. Sabri
Centre for Advanced Materials and Industrial Chemistry (CAMIC)
School of Science
RMIT University
Melbourne, VIC 3001, Australia

S. Balendhran, A. Roberts, K. B. Crozier, N. Syed
School of Physics
The University of Melbourne
Parkville, VIC 3010, Australia
E-mail: kenneth.crozier@unimelb.edu.au

A. Roberts, K. B. Crozier, N. Syed
ARC Centre of Excellence for Transformative Meta-Optical Systems
The University of Melbourne
Parkville, VIC 3010, Australia

K. B. Crozier
Department of Electrical and Electronic Engineering
The University of Melbourne
Parkville, VIC 3010, Australia

The ORCID identification number(s) for the author(s) of this article can be found under https://doi.org/10.1002/adfm.202309342

DOI: 10.1002/adfm.202309342

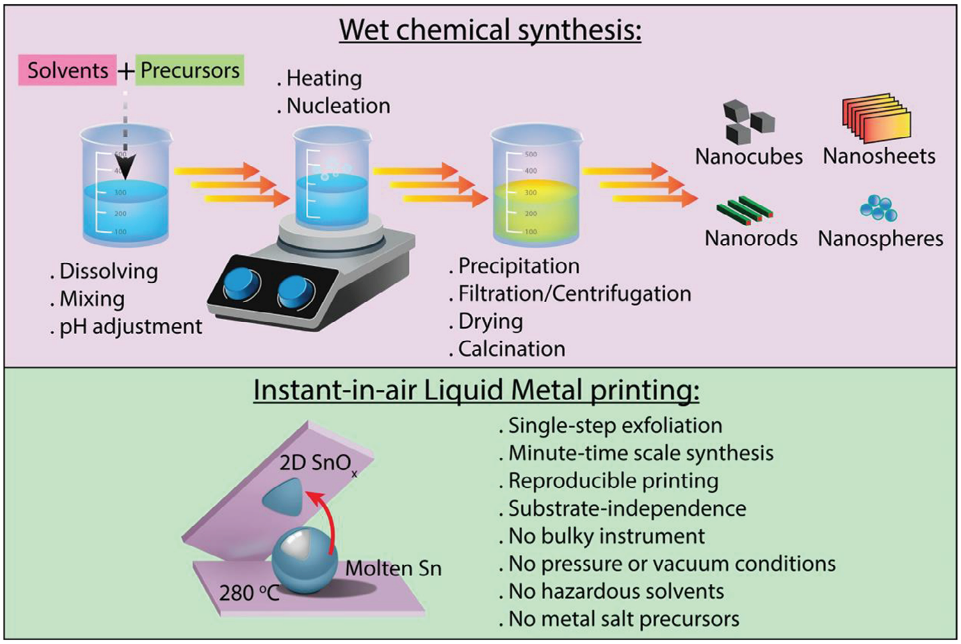

Scheme 1. A schematic comparing conventional methods with the LM printing process for realizing SnO_2 nanostructures. The approach is simple, holds promise for industrial-scale application, and will inspire further research in the community.

sector will require the deployment of robust monitoring equipment to ensure safe operation. Furthermore, from a medical perspective, monitoring ammonia levels in human breath has the potential for non-invasive diagnosis of various diseases.[9–12] Due to these compelling applications, ammonia detection at ppm and sub-ppm levels has become a topic of significant research interest, and the development of robust, low-cost and yet highly sensitive, and selective NH_3 sensors is paramount.

Two-dimensional (2D) materials have been considered as a powerful class of materials in a variety of gas-sensing applications due to their intriguing optical and electronic properties originating from their atomically thin tenuity and ultrahigh surface-to-volume areas.[13] Nanosheets derived from materials with non-layered crystal structures are of particular interest, since they form covalent bonds in all three dimensions and unsaturated dangling bonds on the surface, making the interface chemically active and thus highly suitable for sensing applications.[14,15] The synthesis of various 2D metal oxides utilizing liquid metals (LMs) as reaction platforms has been introduced relatively recently and is gaining considerable attention due to the straightforward deposition process and its ability to produce large and ultra-thin materials with both layered and non-layered structures which is challenging when using conventional exfoliation processes.[16–18] The surface oxide growth on low-temperature LMs is often self-terminating and follows the Cabrera-Mott oxidation process,[16,17,19] and thereby facilitates the formation of oxide nanosheets with a highly reproducible thickness which typically is in the 1–3 nm range. Due to the liquid nature of the underlying metal, the interfacial oxide is found to delaminate with ease, enabling liquid metal printing routes that are straightforward and yet have been demonstrated to reliably produce 2D materials at wafer scales and may have profound possibilities in various conductometric sensing applications. This work reports on the fabrication of liquid metal printed SnO_2 nanosheets which have been employed as active channels in conductometric gas sensing devices.

Tin dioxide (SnO_2) is considered a wide bandgap and *n*-type transparent metal oxide (MOX) of technological importance.[20,21] SnO_2 is a promising candidate for gas sensing owing to its excellent chemical stability and high electrical conductivity.[22,23] However, the performance of pure SnO_2 for NH_3 sensing applications is often poor[24,25] and hence doping and composing SnO_2 with some enhancers had been used to specifically improve its sensitivity.[26,27] So far, the NH_3 gas sensing behavior of LM-derived 2D SnO_2 films has not been reported yet.

As depicted in **Scheme 1**, various SnO_2 nanostructures have been realized via wet chemical synthesis methods with the use of solvents and precursors. These conventional synthesis methods require a synthesis process that can extend to several hours or a few days. Hence, an economical, simple, faster, and reproducible process for making high-performance gas-sensitive layers is long overdue and much needed in the chemical sensor community. In this work, we utilize the LM printing method to harvest ≈2 nm thick SnO_2 nanosheets from the surface of molten tin without the use of any toxic solvents and hazardous chemicals. The whole printing process only takes less than a minute in an ambient environment. As such, the LM printing technique enables a simple and low-cost approach to realize ultrathin SnO_2 nanosheets with highly reproducible quality and areas approaching ≈1 cm^2 Resistive devices are fabricated on 2D SnO_2 nanosheets and operated in amperometric mode to detect NH_3 gas.[28] The amperometric gas sensors (AGSs) are tuned via different external biases to enhance their gas sensing performance. Furthermore, the utilization of optical excitation notably improves the sensitivity and selectivity of the fabricated AGS, boosting the interaction

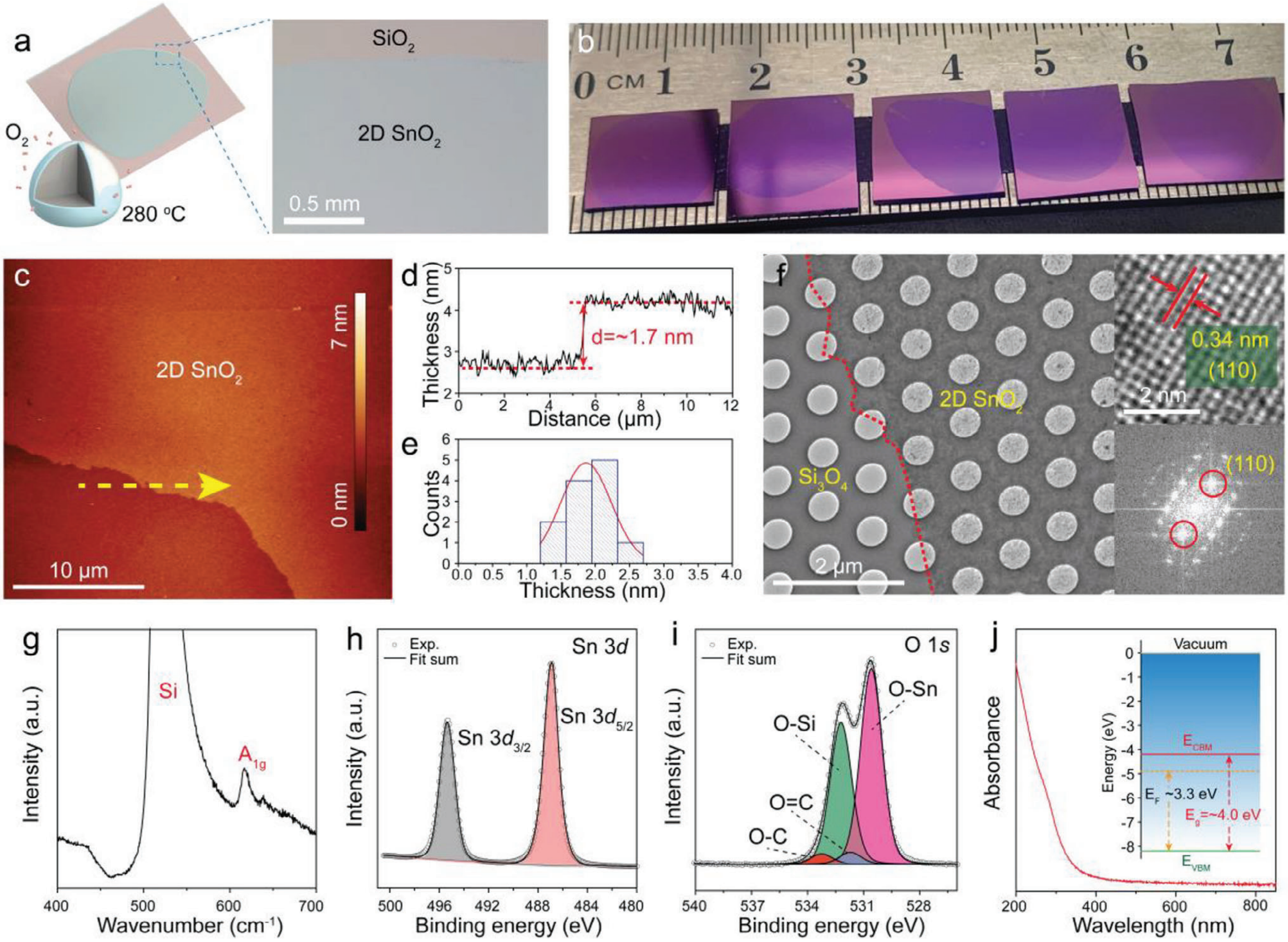

Figure 1. Characterizations of ultrathin 2D tin oxide (SnO_2) obtained using the van der Waal touch printing technique and post-annealing at 450 °C for 15 min in air. a) Schematic illustrating the touch printing technique for isolating 2D tin oxide. Right: optical microscope image of continuous 2D SnO_2 sheet prepared on 300 nm SiO_2/Si substrate, with area of several square millimeters. b) Centimeter-scale 2D films (on 300 nm SiO_2/Si) were frequently obtained, highlighting the consistency of the synthesis process. c) AFM micrograph of 2D SnO_2 nanosheets. d) Height profile along the yellow line of panel c. Thickness analysis at 12 edge locations collected from multiple nanosheets results in an average thickness of 1.9 ± 0.4 nm (standard deviation). f) TEM micrograph of the SnO_2 films, the right top inset indicates lattice fringes of the 2D SnO_2 films and the bottom inset represents the FFT pattern. The red dashed line is used to indicate the edge of 2D SnO_2 on TEM grids. g) Raman spectra of tin oxide printed on SiO_2/Si substrates. h,i) Fitted XPS spectra of the 2D SnO_2 nanosheets for h) Sn 3d core level and i) O 1s core level. j) UV–Vis absorbance spectra and the inset display the constructed band diagram of the 2D SnO_2. The n-type nature of the SnO_2 is evidenced by the measured Fermi level (E_F) being closer to the conduction band minimum (E_{CBM}) than the valence band maximum (E_{VBM}).

between the sensing layers and gas analytes, as well as lowering the required operating temperature of the sensor to 150 °C. Our liquid metal-derived SnO_2-based gas sensors are found to be highly selective toward ammonia molecules over many potential interferential gases while having a very low Limit of Detection (LoD) at parts per billion (ppb) range. The developed sensors exhibited excellent stability even when stored in air over the course of several weeks and also showed reproducible sensing responses for different batches of samples. We have also benchmarked the performance of our novel 2D SnO_2 nanosheets ammonia sensors against commercially available SnO_2 nanoparticles. Moreover, we demonstrate the realization of a prototype flexible NH_3-gas-sensing platform utilizing liquid metal-derived 2D SnO_2 providing opportunities for future wearable gas sensors.

2. Results and Discussion

The synthesis of wafer-scale 2D tin oxide (SnO_x) nanosheets was carried out using a vacuum-free liquid metal-based van der Waal (vdW) transfer technique[17] as illustrated in **Figure 1**a. This is a single-step liquid metal printing route that enables the direct transfer of atomically thin oxides onto suitable substrates.[17,29,30] The exfoliation of 2D SnO_x was performed immediately from the freshly preconditioned tin melted at 280 °C in the ambient atmosphere (see Experimental section). It has been reported that liquid metal-derived SnO_x consists of both tin monoxide (SnO) and tin dioxide (SnO_2) when printing under atmospheric conditions.[29,31] Hence, the 2D SnO_x nanosheets were subjected to post-thermal annealing at 450 °C for 15 min in ambient air in order to obtain the dominant SnO_2 phase which has been validated via various characterizations (as described below). In addition, annealing at a temperature greater than 400 °C is known to enhance the crystalline quality of tin oxide films by minimizing local lattice disorders and decreasing the density of the vacant lattice sites within each crystal, leading to a steady lattice constant of the unit cell.[32,33]

It can be seen from Figure 1b that large-area 2D SnO_2 films are consistently achieved using the LM touch printing process, confirming the reproducibility of this technique. Moreover, laterally large 2D SnO_2 nanosheets with minimal cracks and folds can be deposited on various substrates (e.g., Si_3N_4, glass, PDMS, Ni, GaAs, InP, etc, see Figure S1, Supporting Information), indicating the relative substrate independence of the printing process as well as presenting opportunities for the fabrication of flexible and transparent devices. Atomic force microscopy (AFM) images in Figure 1c and Figures S2 and S3 (Supporting Information) reveal that the 2D SnO_2 sheets are atomically flat and uniform over large areas. From AFM data, no obvious changes in film thickness were observed after annealing. Analysis of sheet thickness at 12 edge locations of 4 different samples indicates that liquid metal printing results in highly reproducible nanosheets with an average thickness of 1.9 ± 0.4 nm for annealed 2D SnO_2 (Figure 1d,e) which is nearly similar to the thickness of as-exfoliated nanosheets with an average thickness of 2.1 ± 0.3 nm (Figure S2a,b, Supporting Information). The root-mean-squared (RMS) and average surface roughness of the annealed 2D SnO_2 nanosheets were found to be 0.78 nm and 0.62 nm, respectively (Figure S3c, Supporting Information). The morphological and crystalline structure of the 2D SnO_2 samples was further characterized by transmission electron microscopy (TEM). The TEM analysis confirms the presence of translucent SnO_2 nanosheets (Figure 1f). The high-resolution TEM (HR-TEM) micrograph and corresponding fast Fourier transform (FFT) reveal a lattice spacing of 0.34 nm, corresponding to (110) plane of the SnO_2 (Figure 1f, insets).[34] This interatomic spacing was frequently observed in TEM analysis of LM-derived 2D SnO_2. Both atomic arrangement and FFT analysis confirm the tetragonal crystal structure of 2D SnO_2.[34] Additional TEM and HRTEM images of 2D SnO_2 have been provided in Figure S3d–g (Supporting Information).

The as-deposited unannealed thin film shows strong Raman modes for both SnO and SnO_2 phases. The SnO modes disappear after annealing, indicating a phase transition to SnO_2 (Figure S4a, Supporting Information). The strong Raman peak observed at ≈617 cm^{-1} (A_{1g} mode) confirms that the SnO_2 has a tetragonal rutile structure with the existence of bridging oxygen vacancies (Figure 1g).[35] X-ray diffraction (XRD) was also conducted to characterize the annealed 2D SnO_2. However, characterizing very thin films with XRD is challenging and hence a multiple-touch printed 2D SnO_2 sample was prepared on glass substrates to increase the XRD signal intensity (Figure S4b, Supporting Information).

The chemical composition and oxidation states of the annealed 2D SnO_2 were analyzed by X-ray photoelectron spectroscopy (XPS), and the spectra of Sn 3d and O 1s are shown in Figure 1h,i. For Sn 3d (Figure 1h), the characteristic doublet peaks located at binding energies of 486.8 and 495.3 eV can be ascribed to Sn $3d_{5/2}$ and Sn $3d_{3/2}$, respectively. It is seen that the peak-to-peak separation between Sn $3d_{5/2}$ and Sn $3d_{3/2}$ is 8.5 eV, which can be attributed to Sn^{4+} states of SnO_2 based on earlier reports.[36] No evidence of the contribution of metallic Sn at ≈485 eV can be observed. Figure 1i displays the deconvoluted O 1s spectra with various oxygen species. The O 1s spectrum observed after annealing showed a peak at ≈530.6 eV which can be assigned to oxygen bound to tin (O—Sn),[36] whilst the remainder are attributed to either the SiO_2 layer on Si substrate (≈532.2 eV) or airborne contaminants (≈531.7 and ≈533.3 eV for C=O and C—O, respectively). The O/Sn ratio was calculated to be 1.3-1.5, implying the oxygen-deficient structure of the produced 2D SnO_2 nanosheets. However, it is important to note that XPS spectra by themselves, when performed ex-situ, do not provide accurate oxygen vacancy identity, nor the precise stoichiometry of binary metal oxides on material surfaces due to the complexity of O 1s deconvolution.[37] Nevertheless, the combination of Raman and XPS studies indicates that the 2D SnO_2 nanosheets feature oxygen-related defects, which have been employed in many sensing applications.

The UV–Vis absorption spectrum of our 2D SnO_2 sample shows pronounced absorption in UV, from which we estimate an optical bandgap of ≈4 eV (≈310 nm, Figure 1j). The inset of Figure 1j elucidates the simplified band diagram based on UV–Vis spectroscopy, valence band XPS (VB-XPS), and photoemission spectroscopy in air (PESA) analysis. PESA revealed that the Fermi level (E_F) of 2D SnO_2 is situated at −4.94 eV (with respect to vacuum) which is consistent with previous literature (Figure S5, Supporting Information).[38] VBXPS indicates the difference of valence band maximum (E_{VBM}) and E_F is ≈ 3.3 eV resulting in the location of the valence band edge at $E_{VBM} = -8.24$ eV with respect to the vacuum (Figure S5b, Supporting Information). Based on the measured direct optical bandgap of $E_g \approx 4$ eV (Figure S5a, Supporting Information) for the SnO_2, we expect the conduction band minimum (E_{CBM}) to be situated at $E_{CBM} = -4.24$ eV indicating the *n*-type semiconducting nature of the synthesized 2D SnO_2 nanosheets.

2.1. Gas Sensing Performance

Previous works have demonstrated different gas-sensing behavior of SnO_2 nanostructures in different shapes and morphologies,[23] but not with ultrathin 2D SnO_2. Hence, we are motivated to use the as-synthesized 2D SnO_2 for gas sensing applications because of its ultra-large surface-to-volume ratio which could greatly enhance the sensor's sensitivity.[39] Its ease of synthesis and reproducibility are also favorable attributes. Furthermore, with MOX-based AGSs, the surface electrical properties of the sensitive layer can be potentially tuned by applying an external bias, which could modify the gas adsorption/detection properties, thereby permitting higher sensitivity.[40] In addition, given the homogeneity over large areas as well as the wide bandgap nature of 2D SnO_2 nanosheets, improvement in gas sensing performance can further be achieved by introducing UV light illumination as an external stimulus to enhance surface reactions. Hence, AGSs based on 2D SnO_2 were developed with and without UV light illumination to enhance the sensitivity and the selectivity performance toward NH_3 gas at relatively lower temperatures (i.e., < 200 °C).

Figure 2a provides a schematic diagram of the device, which has interdigitated electrodes (IDEs) (see Figure S6a,b,

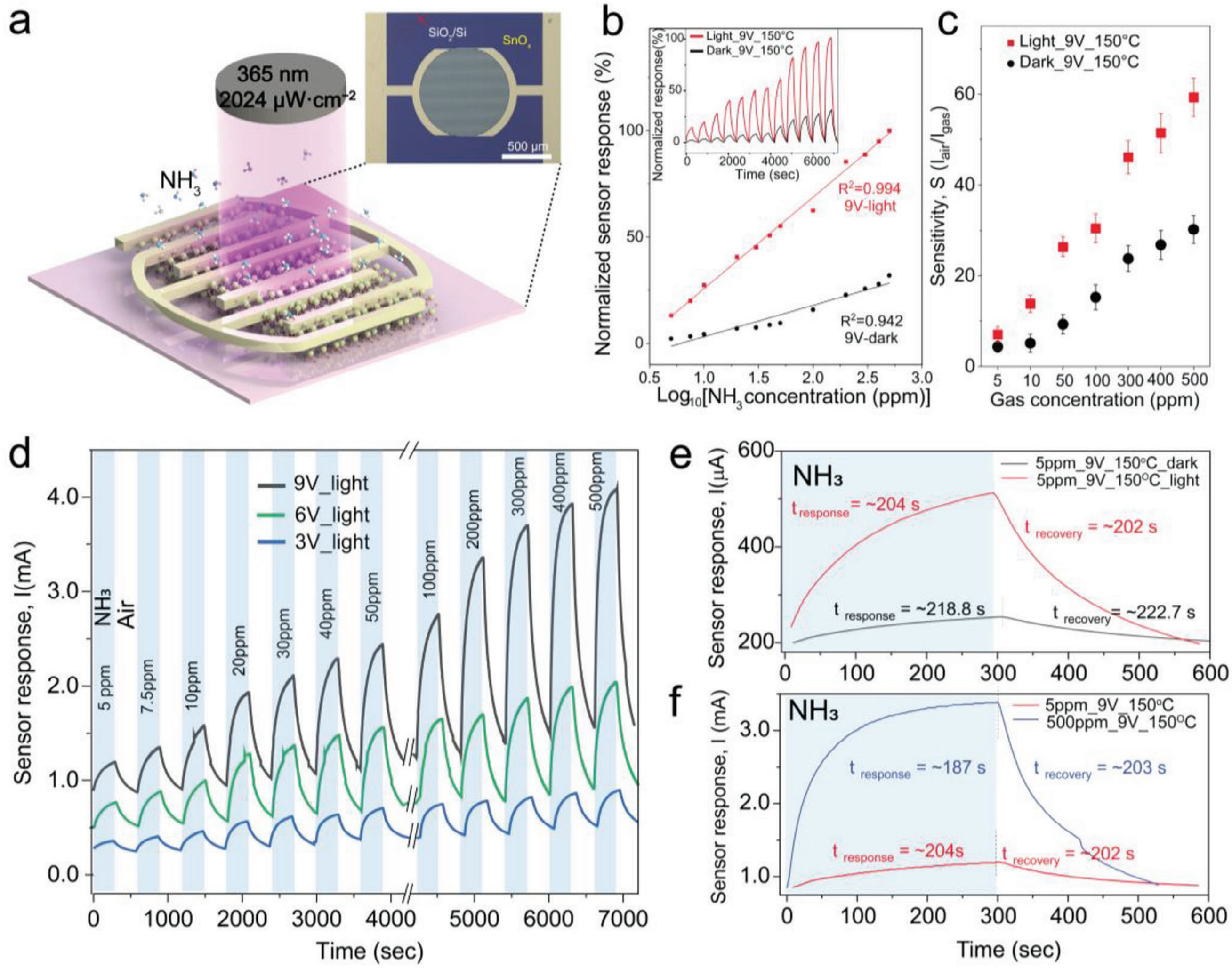

Figure 2. a) The schematic structure of the NH_3 gas sensor utilizing large area SnO_2 film. The inset shows the optical image of the IDE device prepared on 300 nm SiO_2/Si substrate; b) Calibration curves with (red) and without (black) UV illumination obtained from response profiles which show the coefficient of determination (R^2) of 0.994 and 0.942, respectively. c) Sensitivity of 2D SnO_2 gas sensor to different NH_3 concentrations under 9 V applied bias with (red) and without (black) UV illumination. d) Response profiles of light-assisted gas sensing toward different concentrations of NH_3 at an operating temperature of 150 °C under different bias conditions. The break in the time scale is due to a certified cylinder changeover for experiments involving the higher concentration range. e) The sensor response and recovery time under 5 ppm NH_3 concentration with and without UV light. f) The observed response and recovery time of the sensor to 5 ppm and 500 ppm NH_3 under UV illumination.

Supporting Information and Experimental section for more details). The NH_3 sensing performance of SnO_2 thin films was tested using a computer-controlled gas delivery calibration setup. This setup supplied NH_3 gas balanced with air using controlled on–off periods in order to pulse the sensor with different NH_3 concentrations (Figure S6c, Supporting Information). The room temperature gas sensing performance was first evaluated by measuring the sensor response with a constant bias under dark and light-illuminated conditions (Figure S7, Supporting Information). For the latter, UV light with a wavelength of 365 nm and an intensity of 2024 μW cm^{-2} was used. As ultrathin metal oxides often exhibit persistent photoconductivity (PPC) effects.[41] Hence any possible PPC effect after introducing UV illumination in our 2D SnO_2-based gas sensor was minimized by stabilizing the baseline current in dry air for at least 3 hours before conducting any experiments under NH_3 exposure (Figure S8, Supporting Information). Under UV illumination, the sensor response (i.e., the change in current when the device was exposed to 50 parts per million (ppm) NH_3) was enhanced ≈7 times, with other operating conditions being identical. This can be attributed to additional photocarrier generation facilitated by UV excitation in the wide bandgap SnO_2 nanosheets which therefore increases the density of electrons and active sites throughout the surface that can participate in the sensing reaction.[42]

To determine the optimum operating temperature, gas sensing experiments were performed at temperatures ranging from room temperature (RT) to 220 °C. It is clear that the NH_3 sensing behavior is strongly dependent on temperature, with higher output currents at elevated operating temperatures (Figure S9, Supporting Information). Increasing the temperature facilitates the adsorption of oxygen radicals and NH_3 molecules on the active sites of 2D SnO_2 which in turn augments the electron transfer process during gas sensing.[42,43] However, if the temperature increases beyond a certain limit, progressive desorption of the oxygen ionic species arises, hence decreasing the sensor sensitivity.[43] From Figure S9 (Supporting Information), it can be seen that among the temperatures tested, the current takes its highest value when the temperature is ≈220 °C. However, the sensor response saturates for NH_3 concentrations ≥ 300 ppm at an operating temperature ≈220 °C. This suggests that for applications where a broad range of concentrations need to be detected, a lower operating temperature than 220 °C should be used. We find that an operating temperature of 150 °C provides an appropriate balance between sensitivity and operating range. In addition, reduced operating temperature (i.e., at 150 °C) also decreases the probability of additional catalytic activity that could occur in the presence of other gas species.[40]

In Figure 2b, we show plots of the normalized response versus NH_3 concentration (log scale) for our SnO_2 sensors, with and without UV excitation at an operating temperature of 150 °C and under a 9 V bias. Here, we performed sensing experiments with NH_3 varying from 5 to 500 ppm. From the data, the limits of detections (LoDs) were calculated to be ≈9.4 parts per billion (ppb) and 646.1 ppb under illuminated and dark conditions, respectively. The LoD was calculated using the equation $LOD = (3 \times STD_{Noise})/S$, where STD_{noise} is the standard deviation of the baseline in the absence of the analyte gas and S is the slope of the calibration curve.[40,44] Our low LoDs are the result of very high sensitivities of the developed sensor toward NH_3 gas which is greatly enhanced by the UV light excitation. Indeed, the sensor shows high sensitivity to NH_3 concentrations down to 5 ppm, which is well below the concentration of 50 ppm that is designated as the "Permissible Exposure Limit (PEL)" by the Occupational Safety and Health Administration (OSHA) and orders of magnitude below the concentration of 300 ppm that is designated as "Immediately Dangerous to Life or Health (IDLH)" by the U.S. National Institute for Occupational Safety and Health (NIOSH).[45,46] It is also worth noting that the permissible exposure limit of NH_3 to humans is 25 ppm (for 8 hours) and 35 ppm (for 10 minutes) as per the OSHA.[6,45] The sensitivity[47] ($S = \frac{I_{gas}}{I_{air}}$) of the fabricated device for 5 ppm NH_3 concentration are calculated to be ~7.3 and ≈4.3, with and without UV illumination, respectively (Figure 2c). The best NH_3-gas sensing performance of 2D SnO_2 was achieved at 500 ppm with a sensitivity of ≈60 under UV light (Figure 2c). The ability to detect such low NH_3 concentrations at low temperatures enables the tuning of the developed sensors for environmental/emission monitoring, safety leak tests, and handheld non-invasive diagnostic applications.

The dynamic response-recovery curves of NH_3 gas sensing at different operating biases (0.1, 3, 6, and 9 V DC) with and without light were determined at the operating temperature of 150 °C (Figure 2d and Figure S10, Supporting Information). These were assessed by cycling different concentrations of NH_3 gas with 300 sec on and 300 sec off pulses. The SnO_2 sensor demonstrated reversible and reproducible responses at different bias voltages. A small response current was obtained at 0.1 V bias voltage and later the sensor response increased with applied voltages. The largest signal was observed for 500 ppm NH_3 pulse while using an applied bias of 9 V. The SnO_2 sensor also showed a significant response to detect NH_3 over the different concentrations (5 ppm to 50 ppm) under dark conditions (Figure S10b, Supporting Information), with promising current signal outputs for operating at relatively lower power consumption. This mode of operation also has the advantage of not requiring a light source.

The response-recovery characteristics to different concentrations of NH_3 are presented in Figure 2e,f. Response and recovery times were measured as the time required for the sensor to reach 90% of its maximum response magnitude and 10% of its baseline value during the recovery period, respectively.[47] No significant improvement in the response and recovery time has been observed under UV illumination (Figure 2e) in comparison to the dark condition due to a higher kinetic energy barrier for reducing gas molecules like NH_3 as observed in the previous report.[48] Next, the response changes of the gas sensor to maximum and minimum ammonia gas concentrations (5 ppm, and 500 ppm) under UV illumination are shown in Figure 2f. The observed response time for the 5 ppm ammonia concentration is ≈204 s and decreases with increasing ammonia concentration, reaching a value of ≈187s for 500 ppm. The trend of lowering response time and changing kinetics observed from the response profiles indicate that the NH_3 reaction kinetics are mass transport (diffusion) limited at the electrode surface at low concentrations and approaches reaction limited at higher concentrations where the analyte supply is much faster than its consumption and similar analyte concentration exist at the electrode surface and bulk air.[28] The sensor recovery time does not show a significant change with higher NH_3 concentration. The response and recovery times with different applied biases are provided in Table S1 (Supporting Information), which demonstrates improved response and recovery time at lower biases. In addition, it is worth noting that there was a constant drift in the sensor response over time due to reaction kinetics (Figure 2d), in which the drift was observed to reduce with increasing time as the sensor was stabilized. For applications where even faster response and recovery times are desired, short pulses (40 sec on and 40 sec off) of NH_3 gas have been introduced into the gas chamber to obtain fast preliminary gas concentration readings with and without UV light illumination at 9 V applied bias. Figure S11 (Supporting Information) demonstrates a rapid rise and fall of the response currents under short NH_3 exposure signifying practical response-recovery times of less than 30 s.

To gain further insight into the gas sensing performance, the developed SnO_2 sensor was exposed to different concentrations of NH_3 gas in order to test the influence of the previous sensing event on the stability of the next sensing event, known as the sensor memory effect.[40] The memory test sequence was developed with five different NH_3 gas concentrations (labeled as *a*, *b*, *c*, *d*, and *e*) and each concentration was repeated a minimum of three times, where $a = 50$ ppm, $b = 100$ ppm, $c = 200$ ppm, $d = 400$ ppm, and $e = 500$ ppm. **Figure 3**a,b shows the sensor response profiles during the memory test with and without light illumination at optimum operating conditions and 9 V bias. The bar graphs (Figure 3c) represent the average response magnitudes with standard errors. It can be seen that the sensor response magnitude was reproducible for every NH_3 gas concentration examined, regardless of the pre-exposed NH_3

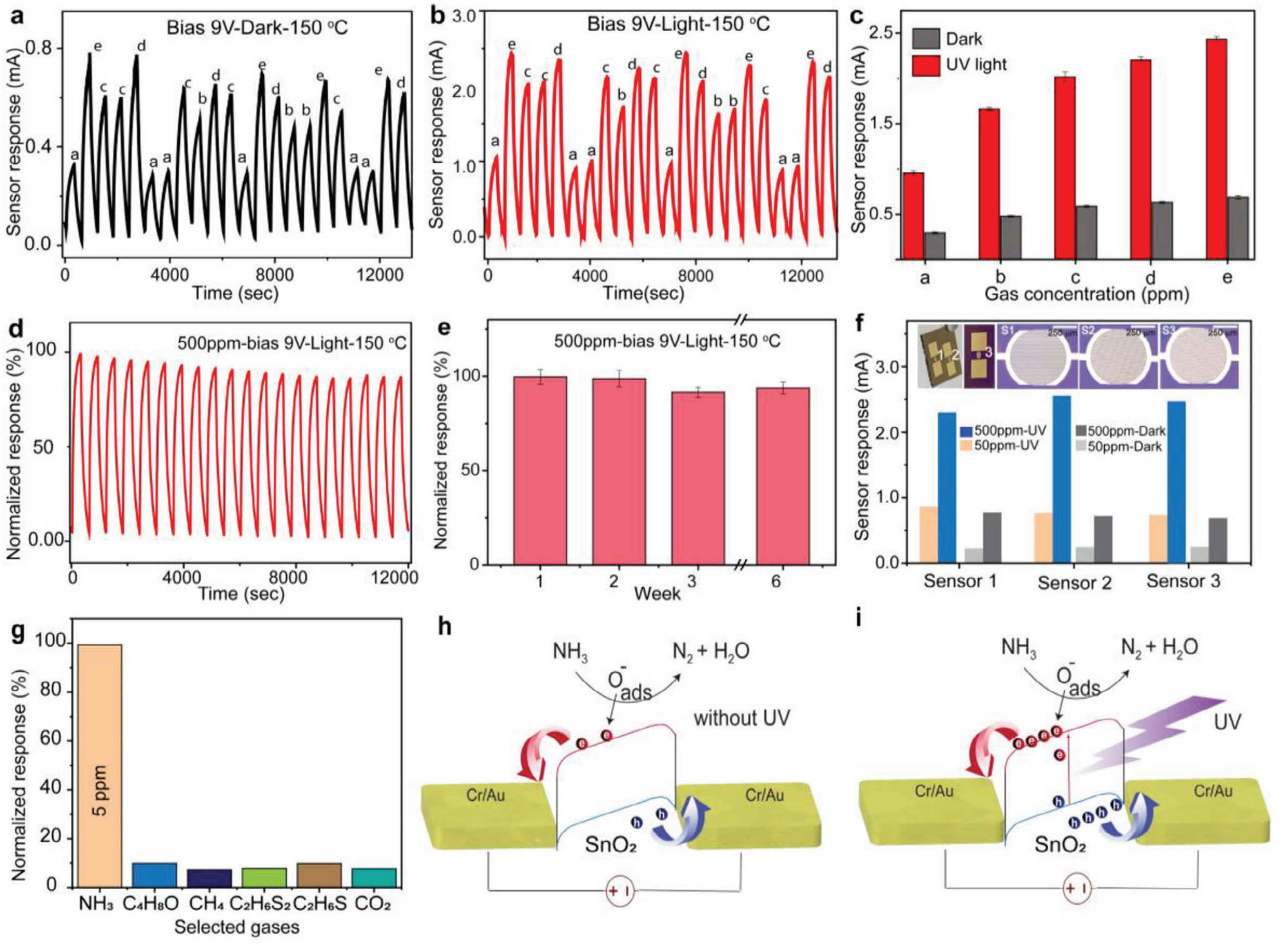

Figure 3. a,b) Dynamic response profile of the 2D SnO_2 gas sensor during memory test conducted at 150 °C at an applied bias of 9 V with and without light illumination. The memory test was conducted at five different NH_3 gas concentrations (labeled as *a*, *b*, *c*, *d*, and *e*) and each concentration was repeated a minimum of four times. c) The bar graphs represent the average response magnitudes during memory tests where the response magnitude is defined as the difference between the output current under the NH_3 gas exposure and that in air. d) Dynamic response–recovery cycles toward 500 ppm of ammonia show stable performance. e) Normalized sensor response toward NH_3 (500 ppm) showing long-term stability over six weeks. f) Different sensors demonstrated excellent reproducibility resulting in similar responses between each fabricated device. g) Normalized response profiles of the gas sensor to different industrially relevant gas species and concentrations under UV light (365 nm, 2024 $\mu W \cdot cm^{-2}$) illumination. h,i) Schematic diagram of the sensing mechanism of AGS based on 2D SnO_2 with and without UV illumination.

concentration to the sensor, indicating negligible memory effects on the developed NH_3 gas sensors.

Figure 3d shows the repeatability of the fabricated sensor which was studied via repeated exposure to 20 cycles for 500 ppm NH_3 concentration at optimized conditions of 150 °C and 9 V bias. The sensor shows minimum baseline drift once it is stabilized. The coefficient of variance (CoV) and repeatability (*R*%) are the figures of merits for the stability analysis of a gas sensor. The CoV and *R*% are determined by $CoV\ (\%) = \frac{\sigma}{\mu} \times 100\%$ and $R\% = 100(\%)\text{-CoV}(\%)$, where σ is the standard deviation of the sensor response and μ is the average sensor response magnitude for a particular gas concentration.[40] The calculated CoV for the SnO_2 sensor toward 500 ppm NH_3 was calculated to be 3.95%, and therefore results in a repeatability of >96.0%, demonstrating excellent reproducibility of sensor response. The sensor also exhibited excellent repeatability for a lower NH_3 concentration (50 ppm) with an R of ≈95% (Figure S12, Supporting Information). Environmental stability is also one of the important parameters of sensors. We therefore tested the response of our sensor (stored in an ambient environment) over the course of six weeks and minor variations in sensor response were observed over the trial periods (Figure 3e), indicating excellent long-term stability. In addition, we have fabricated a number of identical sensors located on different spatial positions of 2D SnO_2. The NH_3 sensing was conducted at optimized conditions (150 °C with an operating bias of 9 V) with and without UV illumination. Different sensors demonstrated excellent reproducibility resulting in reproducible response between each fabricated device (Figure 3f and Figure S13, Supporting Information). Therefore, the consistent deposition of tin oxide offers the opportunity for mass production with a similar response between each fabricated sensor. For comparison, the performance of our novel 2D SnO_2-based ammonia sensors was benchmarked against commercially available SnO_2 nanoparticles (particle size < 100 nm) which were subjected to the same gas sensing test by drop-casting the nanomaterials on identical IDEs. The material characterizations and the ammonia sensing behavior of commercial SnO_2 have been detailed in Figure S14 (Supporting Information). Although commercial SnO_2 nanoparticles exhibited capacity for ammonia sensing, the conventional drop-casting method led to the non-uniform deposition of materials onto the sensor electrodes and hence inconsistent and unreliable performances.

2D SnO_2-based gas sensor was found to be highly selective to NH_3, producing a substantially larger response than for any other contaminant gas species tested. Figure 3g shows the normalized response profiles of the SnO_2-based gas sensor to 5 ppm NH_3 and other possible interferent gases that are commonly used in industry. The cross-interferent gas species that were tested comprised carbon dioxide (CO_2 at 500 ppm), methyl ethyl ketone/MEK (C_4H_8O, at 40.1 ppm), ethyl mercaptan (C_2H_6S at 2.61 ppm), methane (CH_4 at 10 000 ppm), dimethyl disulfide /DMDS ($C_2H_6S_2$ at 5 ppm). In these tests, the sensor was maintained at a temperature of 150 °C with a bias of 9 V under UV light illumination. The concentrations of the interferant gases used in the tests were chosen to be the maximum concentrations expected in the environment and/or industrial processes. It is observed that the sensor response for NH_3 is much greater than for the other gas species tested, indicating minimal cross-sensitivity (Figure S15, Supporting Information). Understanding the effect of moisture on the performance of 2D SnO_2-based sensors is also essential to determine the full potential of these devices. The role of moisture in detecting different target gases has been displayed in Figure S16 (Supporting Information). This was studied by injecting controlled humidity content in the test chamber while keeping the other parameters constant. The normalized sensor response was found to be ≈20% in the presence of ≈18% relative humidity at 25 °C.

To further highlight the novelty of liquid metal printed 2D SnO_2, a prototype flexible NH_3 sensor on polyimide Kapton substrate was fabricated (Figure S17, Supporting Information). The sensor was then subjected to different concentrations of ammonia (5-50 ppm) with UV excitation at an operating temperature of 150 °C and under a 9 V bias. The sensor featured a promising sensing performance with a LoD of ≈ 0.2 ppm and a high repeatability via repeated exposure to 10 cycles of 50 ppm NH_3. This demonstration highlights the potential of LM-printing for realizing wearable sensors. However, further experimental analysis and optimization of the 2D SnO_2-based flexible NH_3 sensor should be considered in future work.

Finally, a summary of the sensing performance reported for various SnO_2-based gas sensors toward ammonia is provided in Table S2 (Supporting Information). As shown, the performance of gas sensors employing pure SnO_2 toward ammonia is inadequate and in most cases, the sensitivity was enhanced by utilizing composites and noble metals making the sensing process more complex. Table S3 (Supporting Information) shows the comparison of NH_3 sensing performance between our SnO_2-based devices and other 2D material-based sensors. It is observed that the reported sensors in the literature lack at least one of the features in terms of production cost, scalability, reproducibility, material thickness, sensor sensitivity, or stability. On the other hand, the printing process of our large area 2D SnO_2 takes less than a minute and is conducted in an ambient environment. The ease of synthesis and reproducibility of the ultrathin metal oxide nanosheets enable large-scale sensor fabrication with identical device performance between different batches which could be easily adoptable for industrial-scale production. Moreover, the printing route also enables depositing 2D SnO_2 on flexible substrates, highlighting the opportunity to realize wearable gas sensors that can find applications in human health monitoring.

2.2. Gas Sensing Mechanism

Figure 3h–i shows the proposed mechanism for the SnO_2-based gas sensors in ammonia exposure with and without UV illumination. The *I–V* characteristics suggest Ohmic contacts between the metal-semiconductor junction of the fabricated devices (Figure S18, Supporting Information). The experiment was carried out in the in-house built chamber with air as the carrier gas, and hence the reaction process involves oxygen and ammonia.[49] The adsorption and oxidation of ammonia on the surface of metal oxides have been studied thoroughly in previous reports.[27,50–53] The sensing behavior could be attributed to the effects of the interactions between NH_3, chemisorbed oxygen ions along with electro- and optoelectro-migration in 2D SnO_2.[42,43,49] The sensing begins with the adsorption of oxygen molecules from the atmosphere onto the surface of 2D SnO_2. The adsorbed oxygens act as electron acceptors and capture the electrons from the conduction band of SnO_2.[27,49] Meanwhile, the temperature can improve the speed of the gas adsorption and further enhance the charge transfer.[43] Next, highly reactive ionized adsorbed oxygen ions (O_x^-), such as O^-, $O_2^-$and $2O^-$, are generated depending on the gas sensor operating temperature and lead to a decrease in the electron density in the conduction band, hence increasing the surface resistance (i.e., reduction in current output).[40,42] When NH_3 gas is injected in, the adsorbed ammonia molecules interact with the negatively charged surface oxygen species. Previous literature has shown oxidation of ammonia leads to the formation of dinitrogen (N_2) with the possible formation of NO and N_2O as side-products.[51,53] However, the temperature dependence of Gibbs free energy and equilibrium constant for reactions of ammonia oxidation leads to the production of N_2 which is much more thermodynamically favorable than generating NO or N_2O.[52] In addition, the production of very stable gas phase molecule of N_2 by the interaction of reducing gas NH_3 with SnO_2 is a low energy demanding exothermic process and thus they are likely to occur at standard experimental conditions.[46,51,53,54] During the oxidation of NH_3, the electrons are released back into the conduction band of SnO_2 which thereby increases the conductivity of the film (Figure 3h). Further, the magnitude of the response current is magnified with larger bias voltages (from 0.1 to 9 V) which results in a decrease in the space charge region and an increased signal output.[40,55]

When the device is subjected to UV illumination, additional photogenerated electron-hole pairs are formed in the *n*-type SnO_2 (Figure 3i).[49,56] These photo-generated electrons react with the adsorbed oxygen in the air and thus generate more ionized $O^-_{2(h\nu)}$

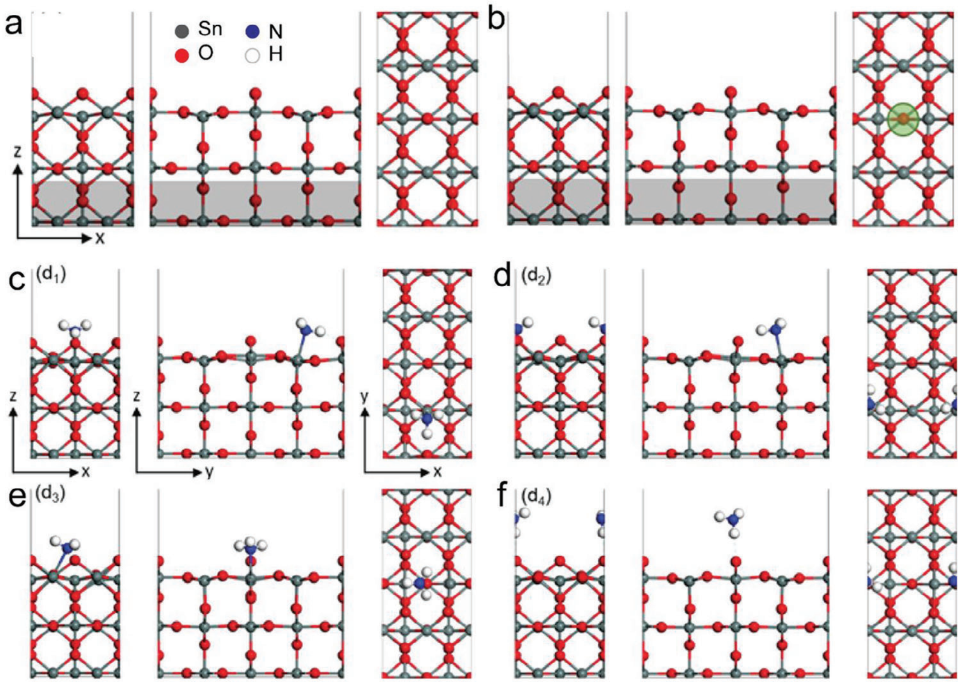

Figure 4. DFT calculated structures of NH_3 adsorption on the 2D SnO_2 surface. Top and side views of the optimized a) pristine SnO_2 (110) and non-stochiometric b) $SnO_2(110)\text{-}V_O$ surfaces. c–f) Top and side views of the most stable configurations of NH_3 absorbed on the $SnO_2(110)\text{-}V_O$ surface.

which ultimately improves the sensing process by reacting with more NH_3 molecules.[40,49,57–59]

$$O_2(\text{gas}) \rightarrow O_2(\text{ads}) \tag{1}$$

$$hv \rightarrow h^+_{hv} + e^-_{hv} \tag{2}$$

$$O_2(\text{ads}) + e^-_{hv} \rightarrow O^-_2(\text{ads}) \tag{3}$$

$$NH_3(\text{gas}) \rightarrow NH_3(\text{ads}) \tag{4}$$

$$2NH_3(\text{ads}) + 3O^-_{2(\text{ads})} \leftrightarrow N_2(g) + 3H_2O(g) + 6e^- \tag{5}$$

To help understand the sensing mechanism of NH_3 on the 2D SnO_2 surface, density functional theory (DFT) calculations and ab initio molecular dynamics (AIMD) simulations were performed for the interaction of NH_3 with defect surfaces of $SnO_2(110)\text{-}V_O$ (**Figure 4**). The (110) facet was selected as it is the most thermodynamically stable surface[60,61] and is consistent with our HRTEM observations (details are provided in the Experimental section).

The preferred binding orientations on the non-stochiometric surface have been presented in Table S4 (Supporting Information) with the binding energy (E_{ads}, eV) and key bond distances (d, Å) of the four stable orientations of NH_3 adsorbed on the SnO_2 surface. Both chemisorption and physisorption approaches were considered to investigate the nature of adsorption. Generally, chemisorption is adsorption with bonding while physisorption is adsorption without bonding. For three of the orientations (Figure 4c–e), NH_3 chemisorbs on the surface with E_{ads} values of −1.49 eV (d_1), −1.41 eV (d_2) and −0.98 eV (d_3). The negative adsorption energy indicates thermodynamic stability and $E_{\text{ads}} < 0$ infers that the adsorption occurred spontaneously. In terms of energy, the d_1 model is the most stable and probable adsorption structure where NH_3 adsorbs to a surface Sn atom via the N atom; the binding is stabilized via the formation of a H-bond between the H of NH_3 and a surface O atom that is adjacent to the defect site. This adsorption geometry of d_2 is similar, except the hydrogen bond is formed with a surface O that is further away from the defect site but there is no H-bond formed. For d_3, the NH_3 bonds to a surface Sn atom in the defect site and results in relatively weaker E_{ads}. For structure d_4, NH_3 is physisorbed on the surface with a BE of −0.21 eV (Figure 4f). In this case, NH_3 is physisorbed on the surface, forming a hydrogen bond between one of the H atoms and an outermost surface O atom. The DFT signifies that there is transfer of charge from the adsorbate to the surface, indicating that NH_3 acts as a charge donor. This charge transfer is stronger when the E_{ads} is greater. Overall, the DFT confirms that the NH_3 adsorption mechanism on the surface of 2D SnO_2 is thermodynamically favorable and dominated by chemisorption. Furthermore, the adsorption of NH_3 molecules induced the charge density redistribution where NH_3 donates electrons in the SnO_2 surface which is consistent with our proposed mechanism.

3. Conclusion

We have demonstrated an efficient gas sensor based on 2D SnO_2 nanosheets with enhanced sensitivity and strong selectivity toward NH_3 gas. The ultra-thin 2D SnO_2 nanosheets were synthesized using a facile liquid metal-based synthesis route with a lateral area of over 1 cm^2 in a highly repeatable and reproducible manner consistent with wafer-scale production scalability. The large area 2D SnO_2 planes consisting of a few unit-cell-thick layers offer plenty of room for the adsorption of NH_3 molecules on the surface. The reproducible deposition of tin oxide offers the opportunity for mass production of sensing devices with highly reproducible responses between each fabricated sensor. The developed sensors were systematically studied with a combination of external bias, optical (UV) excitation, and temperature as external sensor stimuli to improve the sensitivity and the selectivity of the device toward NH_3 gas. The unique surface properties of 2D SnO_2 enable the detection of NH_3 gas down to 5 ppm with a LoD of less than 10 ppb. The sensors featured high repeatability, large dynamic range, low detection limits, insignificant drift, and memory effects. Liquid metal-derived ultrathin SnO_2 nanosheets also demonstrated a high cross-selectivity to different gases, including both organic and inorganic species. The sensing devices exhibited good stability under both ambient storage and repetitive sensing activity over several months, rendering a promising technique for stable and reliable detection of NH_3. Ab initio DFT calculations demonstrated that the NH_3 adsorption mechanism is dominated by chemisorption with a charge transfer occurring into the 2D SnO_2 nanosheets, even at room temperature. In addition, we also provided a proof of concept for flexible ammonia sensors by fabricating a prototype gas-sensing device on a polyimide (Kapton) substrate, signposting opportunities for future work. Overall, the results support the realization of an economical and efficient NH_3-gas-sensing approach which could invite further investigation of liquid metal-based synthesis platforms for next-generation sensing applications.

4. Experimental Section

Materials: Elemental tin (99.9%) was purchased from Roto Metal. All solvents and SnO_2 nanopowder ($\leq$100 nm) were obtained from Sigma-Aldrich and used as received. Flexible polyimide Kapton films were obtained from Premier Lab Supply. All gas cylinders were purchased from BOC. Two cylinders of 0.01% and 0.1% NH_3 (balanced in nitrogen) were used in the experiments.

Liquid Metal Printing Process of 2D Tin Oxide Nanosheets: A van der Waal (vdW) touch printing technique was used to synthesize ultrathin tin oxide nanosheets by adapting previous reports.[17,29] The synthesis process was performed under ambient conditions. Bulk tin metal was melted at 280 °C and squeezed between two glass slides to remove pre-existing oxide layers with possible air-borne contaminants.[29] After preconditioning steps, the freshly formed oxide skins were exfoliated by gently touching the surface with a desired substrate pre-heated at 280 °C. Next, the obtained nanosheets were subjected to post-annealing at 450 °C for 15 min in ambient air.

Characterizations of 2D Tin Oxide Nanosheets: A Thermo Scientific monochromatic Al K_α XPS spectrometer ($h\nu \approx 1486.6$ eV) equipped with a concentric hemispherical analyzer was utilized to conduct the XPS analysis. The XPS data was processed with CasaXPS software. Optical images were obtained using a Leica DM2500 optical microscope. The thickness analysis and surface morphology of 2D tin oxide nanosheets were acquired with a Bruker Dimension Icon AFM operating under ScanAsyst-air mode. The AFM images were then analyzed with Gwyddion 2.55 software. TEM images were taken from a JEOL JEM-2100F TEM operating at an acceleration voltage of 200 kV equipped with a Gatan OneView camera. Gatan Microscopy suite software was utilized to analyze the data. TEM samples were prepared by directly printing the tin oxide sheets onto thermally and mechanically robust silicon nitride membrane window grids (Si_3N_4 grids, Ted Pella, 21587-10). SEM images were taken from a Nova Nano SEM with an accelerating voltage of 5 kV. SEM samples were prepared on silicon substrates. XRD was carried out using a Bruker D4 diffractometer with Cu Kα radiation (1.5418 Å). XRD samples were prepared on glass substrates. UV–Vis measurements were acquired from 2D SnO_x samples prepared on quartz utilizing a Cary 60 UV–vis spectrophotometer. PESA (Riken Keiki AC-2) was utilized to study the VB energy levels at a power of 500 nW. Raman spectra of the synthesized and annealed 2D SnO_x were carried out using a Raman spectrometer (Horiba Scientific LabRAM HR Evolution) equipped with a 532 nm laser source and 1800 mm^{-1} grating.

Device Fabrication: 300-nm-thick SiO_2/Si substrates were sequentially cleaned with acetone, 2-propanol, and Mili-Q water, and blow-dried with compressed air. Then, 2D SnO_2 nanosheets were printed on the SiO_2/Si substrates utilizing the method discussed above. Interdigital electrodes (IDEs) were fabricated on 2D SnO_2 nanosheets with 45 pairs of electrodes with 5 µm gaps between them. The overall area of IDEs was 850 µm × 850 µm. The devices were fabricated via a photolithography process. First, the AZ 5214-E photoresist was spin-coated on samples prior to the electrode patterning using a Maskless Aligner – Heildberg MLA150. An e-beam evaporator (PVD75 – Kurt J. Lesker) was then employed to deposit Cr(10 nm)/Au (100 nm) electrodes, followed by a lift-off process in acetone to remove the photoresist residue. Similar IDEs were deposited on bare SiO_2/Si substrates for fabricating SnO_2 nanoparticle-based gas sensors. 0.1 g commercial SnO_2 nanopowders (Sigma) were suspended in 20 mL ethanol and the mixture was sonicated for 1 h. Subsequently, 10 µL of this suspension was drop-casted on IDEs preheated at 50 °C and the sensors were then mildly annealed at 150 °C for 30 min to improve the contact between electrodes and SnO_2 particles. Shadow mask technique was used to fabricate flexible gas sensors. DCT Laser Micromachining was employed to cut out the pre-designed masks with IDE electrodes with 300 µm gaps between them. 2D tin oxide nanosheets were prepared on flexible Kapton films by utilizing the touch printing method and subjected to post-annealing at 300 °C for 15 min in ambient air. Metal contact deposition was then carried out using an e-beam evaporator (PVD75 – Kurt J. Lesker).

Gas Testing Setup: The gas sensing experiments were carried out in a custom-made Teflon chamber with an in-built optically polished quartz window lid. Fabricated sensors were mounted on a ceramic heating bed. UV source (365 nm LED, Edmund Optics) with 2024 µW cm^{-2} incident power was used for photoactivation. PM16-140 power meter (Thorlabs) was used for the light intensity calibration.

The sensors were exposed to an environment with different NH_3 concentrations ranging from 5 to 50 ppm (standard cubic centimeters per minute or mL min^{-1}) by using a low-concentration certified cylinder of NH_3 (0.01%). Another certified cylinder (0.1% NH_3) gas was utilized for high-concentration sensing experiments (i.e., 50–500 ppm). This allowed for minimizing dilution errors while maintaining the consistent total flow rate of 200 sccm. The baseline was stabilized by exposing the sensor to dry air (200 sccm) for at least 2 h before conducting any new experiments. Different gas species, including carbon dioxide (CO_2), methyl ethyl ketone/MEK (C_4H_8O), ethyl mercaptan (C_2H_6S), methane (CH_4), dimethyl disulfide/DMDS ($C_2H_6S_2$), were used to determine the selectivity (in the ppm range) of the sensors. The sensors were also tested against 18% relative humidity at 25 °C.

The gas flow rate and gas concentration in the sensing chamber were controlled and monitored by exploiting a computer-controlled multichannel mass flow controller (MFC) system. The sensing performances were conducted at different bias voltages (0.1–9 V) with and without light illumination. The temperature of the sensor was varied from RT to 220 °C to find the optimum operating temperature. The response magnitude was defined as the difference between the output current under the NH_3 gas exposure period (I_{gas}) and that in the air (I_{air}): $\Delta I = I_{gas} - I_{air}$. The sensitivity (S) was defined as $S = \frac{I_{gas}}{I_{air}}$.

DFT Calculations: The density functional theory (DFT) was performed utilizing the Vienna ab initio Simulation Package (VASP).[62,63] The SnO_2 (110) surface was cleaved from bulk SnO_2 with cell dimensions of 4.83 × 4.83 × 3.24 Å, which agrees with the previous DFT study.[64] The generalized-gradient approximation (GGA) was employed with the Perdew-Burke-Ernzerhof (PBE)[65] exchange-correlation functional and projector augmented wave (PAW)[66] method to define the ion-electron interaction. An energy cutoff of 400 eV was used, with a *k*-point mesh of 5 × 2 × 1 to sample the Brillouin zone. van der Waals forces were accounted for by the Grimme DFT-D3 approach.[67]

A [2×2] model of stoichiometric SnO_2 was used, having lattice parameters of $a = 6.49$ Å and $b = 13.67$ Å (Figure 4a). A vacuum spacer of 14 Å was added in the *z*-direction to minimize interactions between adjacent cells after the application of periodic boundary conditions. However, due to the presence of oxygen vacancies in the structure of 2D SnO_2 (as discussed in XPS and Raman), a more realistic model to represent the experimental scenario is considered for DFT where one of the topmost surface O atoms was removed from the stoichiometric surface, creating the SnO_2 (110)-V_O surface (Figure 4b) to observe the effect of oxygen vacancies on ammonia interaction with SnO_2. The NH_3 molecule was optimized in a 15 × 15 ×15 Å sized cell.[65] To model the adsorption of NH_3 on the surface, the adsorbate was initially placed ≈3 Å above each surface in different adsorption sites and orientations. The atoms in the bottom surface layer (as shaded in grey in Figure 4a,b) were fixed while all other atoms were allowed to relax until the total energy of the system was converged to 1×10^{-6} eV and the Hellman—Feynman force on each relaxed atom was less than -0.01 eV $Å^{-1}$.

AIMD simulations were performed at 298 K with a time step of 0.5 fs for up to 1 ps using the Verlet algorithm to integrate the equations of motion, with the temperature being controlled by the Nose thermostat. A geometry optimization was then run on the final structure followed by a vibrational frequency calculation, performed by diagonalizing a finite difference construction of the Hessian matrix with displacements of 0.015 Å, allowing only the adsorbate atoms to relax.

A geometry optimization was then undertaken on the final structure followed by a vibrational frequency calculation, performed by diagonalizing a finite difference construction of the Hessian matrix with displacements of 0.015 Å, allowing only the adsorbate atoms to relax. The whole system was first optimized to calculate its physical properties. Then through the difference between the reconstructed surface and the whole system, the adsorption energy and contribution from charge transfer were obtained.

When building the model of NH_3 adsorption on a SnO_2(110)-V_O surface, four possible models were developed with the N atom connecting to the surface. The adsorption energies of the NH_3 gas molecules on the SnO_2 surface were calculated as $E_{ads} = (E_{gas+surface} - E_{surface} - E_{gas})$, where $E_{gas+surface}$, $E_{surface}$, and E_{gas} are the total energies of the adsorbed system, the isolated surface, and the isolated NH_3, respectively. Bader partial charges on individual atoms were calculated using the method described by Henkelman et al.[68] These partial charges were used to determine the charge transfer (D_q), and thus whether the adsorbate behaves as a charge donor or acceptor. The charge transfer was calculated for each system using the following formula, $D_q = q_{qads}$, where q_{ads} is the charge of the individual atoms in the adsorbate. Positive values of D_q indicated that the adsorbate acts as a charge donor, while negative values suggested the adsorbate acts as a charge acceptor.

Supporting Information

Supporting Information is available from the Wiley Online Library or from the author.

Acknowledgements

The authors would also like to thank the RMIT Microscopy and Microanalysis Facility (RMMF) and the Micro Nano Research Facility (MNRF). The authors also acknowledge Dr. Irfan Haider Abidi and Dr. Hank Han (RMIT University) for sharing SnO_2 nanoparticles and experience. N. Syed recognizes the support of a McKenzie Postdoctoral Fellowship from the University of Melbourne. Y. Sabri acknowledges funding received from the Cooperative Research Centres Projects (CRC-P) Grant (CRCPXII000111). T. Daeneke and C. K. Nguyen acknowledge funding received from the Australian Research Council's (ARC) DECRA program (DE190100100). T. Daeneke also acknowledges funding received from the ARC via the discovery program (DP220101923). This research was also supported, in part, by the Australian Research Council (ARC) Centre of Excellence for Transformative Meta-Optical Systems (TMOS, CE200100010).

Open access publishing facilitated by The University of Melbourne, as part of the Wiley - The University of Melbourne agreement via the Council of Australian University Librarians.

Conflict of Interest

The authors declare no conflict of interest.

Data Availability Statement

The data that support the findings of this study are available from the corresponding author upon reasonable request.

Keywords

2D materials, ammonia sensing, DFT calculations, liquid metal, tin oxide

Received: August 8, 2023
Revised: October 8, 2023

---

[1] G. Neri, *Chemosensors* **2015**, *3*, 1.
[2] D. R. Macfarlane, P. V. Cherepanov, J. Choi, B. H. R. Suryanto, R. Y. Hodgetts, J. M. Bakker, F. M. Ferrero Vallana, A. N. Simonov, *Joule* **2020**, *4*, 1186.
[3] L. Greenjr, *Int. J. Hydrog. Energy* **1982**, *7*, 355.
[4] M. Aziz, A. T. Wijayanta, A. B. D. Nandiyanto, *Energies* **2020**, *13*, 3062.
[5] R. Lan, J. T. S. Irvine, S. Tao, *Int. J. Hydrog. Energy* **2012**, *37*, 1482.
[6] D. Kwak, Y. Lei, R. Maric, *Talanta* **2019**, *204*, 713.
[7] A. Joshi, S. A. Gangal, S. K. Gupta, *Sens. Actuators, B* **2011**, *156*, 938.
[8] B. Timmer, W. Olthuis, A. V. D. Berg, *Sens. Actuators, B* **2005**, *107*, 666.
[9] T. Hibbard, A. J. Killard, *Crit. Rev. Anal. Chem.* **2011**, *41*, 21.
[10] J. P. Ong, A. Aggarwal, D. Krieger, K. A. Easley, M. T. Karafa, F. Van Lente, A. C. Arroliga, K. D. Mullen, *Am. J. Med.* **2003**, *114*, 188.
[11] D. J. Kearney, T. Hubbard, D. Putnam, *Dig. Dis. Sci.* **2002**, *47*, 2523.
[12] P. Ma, J. Li, Y. Chen, B. A. Zhou Montano, H. Luo, D.i Zhang, H. Zheng, Y. Liu, H. Lin, W. Zhu, G. Zhang, H. Mao, J. Yu, Z. Chen, *Microw. Opt. Technol. Lett.* **2023**, *65*, 1475.
[13] X. Liu, T. Ma, N. Pinna, J. Zhang, *Adv. Funct. Mater.* **2017**, *27*, 1702168.
[14] F. Wang, Z. Wang, T. A. Shifa, Y. Wen, F. Wang, X. Zhan, Q. Wang, K. Xu, Y. Huang, L. Yin, C. Jiang, J. He, *Adv. Funct. Mater.* **2017**, *27*, 1603254.
[15] N. Zhou, R. Yang, T. Zhai, *Mater. Today Nano* **2019**, *8*, 100051.
[16] P. Aukarasereenont, A. Goff, C. K. Nguyen, C. F. Mcconville, A. Elbourne, A. Zavabeti, T. Daeneke, *Chem. Soc. Rev.* **2022**, *51*, 1253.
[17] A. Zavabeti, J. Z. Ou, B. J. Carey, N. Syed, R. Orrell-Trigg, E. L. H. Mayes, C. Xu, O. Kavehei, A. P. O'mullane, R. B. Kaner, K. Kalantar-Zadeh, T. Daeneke, *Science* **2017**, *358*, 332.
[18] B. J. Carey, J. Z. Ou, R. M. Clark, K. J. Berean, A. Zavabeti, A. S. R. Chesman, S. P. Russo, D. W. M. Lau, Z.-Q. Xu, Q. Bao, O. Kavehei, B. C. Gibson, M. D. Dickey, R. B. Kaner, T. Daeneke, K. Kalantar-Zadeh, *Nat. Commun.* **2017**, *8*, 14482.
[19] N. Cabrera, N. F. Mott, *Rep. Prog. Phys.* **1949**, *12*, 163.
[20] S. Baco, A. Chik, F. M. Yassin, *J. Sci. Technol.* **2012**, *4*, https://publisher.uthm.edu.my/ojs/index.php/JST/article/view/468.

[21] M. Karmaoui, A. B. Jorge, P. F. McMillan, A. E. Aliev, R. C. Pullar, J. A. Labrincha, D. M. Tobaldi, *ACS Omega* **2018**, *3*, 13227.
[22] M. Batzill, U. Diebold, *Prog. Surf. Sci.* **2005**, *79*, 47.
[23] S. Das, V. Jayaraman, *Prog. Mater. Sci* **2014**, *66*, 112.
[24] I. Rawal, *RSC Adv.* **2015**, *5*, 4135.
[25] W. Guo, X. Duan, Y. Shen, K. Qi, C. Wei, W. Zheng, *Phys. Chem. Chem. Phys.* **2013**, *15*, 11221.
[26] R. Ramanathan, S. Nagarajan, V. Bonu, P. Patel, S. Jamdar, H. C. Barshilia, R. C. Mallik, *ACS Appl. Nano Mater* **2023**, *6*, 7873.
[27] S. Xu, K. Kan, Y. Yang, C. Jiang, J. Gao, L. Jing, P. Shen, L.i Li, K. Shi, *J. Alloys Compd.* **2015**, *618*, 240.
[28] J. R. Stetter, J. Li, *Chem. Rev.* **2008**, *108*, 352.
[29] T. Daeneke, P. Atkin, R. Orrell-Trigg, A. Zavabeti, T. Ahmed, S. Walia, M. Liu, Y. Tachibana, M. Javaid, A. D. Greentree, S. P. Russo, R. B. Kaner, K. Kalantar-Zadeh, *ACS Nano* **2017**, *11*, 10974.
[30] R. S. Datta, N. Syed, A. Zavabeti, A. Jannat, M.d Mohiuddin, M.d. Rokunuzzaman, B. Yue Zhang, M.d. A. Rahman, P. Atkin, K. A. Messalea, M. B. Ghasemian, E. D. Gaspera, S. Bhattacharyya, M. S. Fuhrer, S. P. Russo, C. F. Mcconville, D. Esrafilzadeh, K. Kalantar-Zadeh, T. Daeneke, *Nat. Electron.* **2020**, *3*, 51.
[31] P. Atkin, R. Orrell-Trigg, A. Zavabeti, N. Mahmood, M. R. Field, T. Daeneke, I. S. Cole, K. Kalantar-Zadeh, *Chem. Commun.* **2018**, *54*, 2102.
[32] J. X. Zhou, M. S. Zhang, J. M. Hong, J. L. Fang, Z. Yin, *Appl. Phys. A* **2005**, *81*, 177.
[33] A. Kar, J. Yang, M. Dutta, M. A. Stroscio, J. Kumari, M. Meyyappan, *Nanotechnol* **2009**, *20*, 065704.
[34] W. Wan, Y. Li, X. Ren, Y. Zhao, F. Gao, H. Zhao, *Nanomaterials* **2018**, *8*, 112.
[35] L. Z. Liu, T. H. Li, X. L. Wu, J. C. Shen, P. K. Chu, *J. Raman Spectrosc.* **2012**, *43*, 1423.
[36] M. Kwoka, L. Ottaviano, M. Passacantando, S. Santucci, G. Czempik, J. Szuber, *Thin Solid Films* **2005**, *490*, 36.
[37] H. Idriss, *Surf. Sci.* **2021**, *712*, 121894.
[38] M. N. Islam, M. O. Hakim, *J. Mater. Sci. Lett.* **1986**, *5*, 63.
[39] N. Yamazoe, *Sens. Actuators B: Chem.* **1991**, *5*, 7.
[40] E. K. Alenezy, Y. M. Sabri, A. E. Kandjani, D. Korcoban, S. S. A. Abdul Haroon Rashid, S. J. Ippolito, S. K. Bhargava, *ACS Sens.* **2020**, *5*, 3902.
[41] G. Bahuguna, I. Mondal, M. Verma, M. Kumar, S. Bhattacharya, R. Gupta, G. U. Kulkarni, *ACS Appl. Mater. Interfaces* **2020**, *12*, 37320.
[42] G. H. Mhlongo, D. E. Motaung, F. R. Cummings, H. C. Swart, S. S. Ray, *Sci. Rep.* **2019**, *9*, 9881.
[43] Y. Wang, Q. Mu, G. Wang, Z. Zhou, *Sens. Actuators B: Chem.* **2010**, *145*, 847.
[44] H. Tang, L. N. Sacco, S. Vollebregt, H. Ye, X. Fan, G. Zhang, *J. Mater. Chem. A* **2020**, *8*, 24943.
[45] National Research Council, *Committee on Acute Exposure Guideline Levels. Acute Exposure Guideline Levels for Selected Airborne Chemicals*, *6*. National Academies Press, USA **2008**, 2.
[46] X.u Liu, N. Chen, B. Han, X. Xiao, G. Chen, I. Djerdj, Y. Wang, *Nanoscale* **2015**, *7*, 14872.
[47] J. Z. Ou, W. Ge, B. Carey, T. Daeneke, A. Rotbart, W. Shan, Y. Wang, Z. Fu, A. F. Chrimes, W. Wlodarski, S. P. Russo, Y. X. Li, K. Kalantar-Zadeh, *ACS Nano* **2015**, *9*, 10313.
[48] D. J. Late, Y.-K. Huang, B. Liu, J. Acharya, S. N. Shirodkar, J. Luo, A. Yan, D. Charles, U. V. Waghmare, V. P. Dravid, C. N. R. Rao, *ACS Nano* **2013**, *7*, 4879.
[49] H. Chen, Y. Chen, H. Zhang, D. W. Zhang, P. Zhou, J. Huang, *Adv. Funct. Mater.* **2018**, *28*, 1801035.
[50] X. Jiang, Y. Zhen, Y. Feng, Z. Yang, Z. Qin, *J. Alloys Compd.* **2023**, *938*, 168520.
[51] F. Shao, M. W. G. Hoffmann, J. D. Prades, J. R. Morante, N. López, F. Hernández-Ramírez, *J. Phys. Chem. C* **2013**, *117*, 3520.
[52] D. Punetha, S. K. Pandey, *IEEE Sens. J.* **2020**, *20*, 14617.
[53] L. Chmielarz, M. Jablonska, *RSC Adv.* **2015**, *5*, 43408.
[54] R. Sankar Ganesh, E. Durgadevi, M. Navaneethan, V. L. Patil, S. Ponnusamy, C. Muthamizhchelvan, S. Kawasaki, P. S. Patil, Y. Hayakawa, *J. Alloys Compd.* **2017**, *721*, 182.
[55] E. H. Rhoderick, *Rev. Phys. Tech.* **1970**, *1*, 81.
[56] O. Lopez-Sanchez, D. Lembke, M. Kayci, A. Radenovic, A. Kis, *Nat. Nanotechnol.* **2013**, *8*, 497.
[57] P. Nakarungsee, S. Srirattanapibul, C. Issro, I.-M. Tang, S. Thongmee, *Sens. Actuator A Phys.* **2020**, *314*, 112230.
[58] J. Li, D. Gu, Y. Yang, H. Du, X. Li, *Front. Mater.* **2019**, *6*, 158.
[59] E. Espid, F. Taghipour, *Crit. Rev. Solid State Mater. Sci.* **2017**, *42*, 416.
[60] D. Wang, Y. Chen, Z. Liu, L. Li, C. Shi, H. Qin, J. Hu, *Sens. Actuators, B* **2016**, *227*, 73.
[61] X. Wang, H. Qin, Y. Chen, J. Hu, *J. Phys. Chem. C* **2014**, *118*, 28548.
[62] G. Kresse, J. Furthmüller, *Phys. Rev. B* **1996**, *54*, 11169.
[63] G. Kresse, J. Furthmüller, *Comput. Mater. Sci.* **1996**, *6*, 15.
[64] Y. Sun, S. Sun, Y. Zheng, Z. Zhang, T. Hou, H. Du, J. Wang, *Appl. Surf. Sci.* **2021**, *570*, 151110.
[65] J. P. Perdew, K. Burke, M. Ernzerhof, *Phys. Rev. Lett.* **1996**, *77*, 3865.
[66] P. E. Blöchl, *Phys. Rev. B* **1994**, *50*, 17953.
[67] S. Grimme, J. Antony, S. Ehrlich, H. Krieg, *J. Chem. Phys.* **2010**, *132*, 154104.
[68] G. Henkelman, A. Arnaldsson, H. Jónsson, *Comput. Mater. Sci.* **2006**, *36*, 354.